Astri Nore

The effect of turbulence on the oxygen uptake of water

Master's thesis in Energy and Environmental Engineering
Supervisor: R. Jason Hearst
Co-supervisor: Pim Bullee
June 2022

NTNU
Norwegian University of
Science and Technology

Astri Nore

The effect of turbulence on the oxygen uptake of water

Master's thesis in Energy and Environmental Engineering
Supervisor: R. Jason Hearst
Co-supervisor: Pim Bullee
June 2022

Norwegian University of Science and Technology
Faculty of Engineering
Department of Energy and Process Engineering

NTNU
Kunnskap for en bedre verden

DEPARTMENT OF ENERGY AND PROCESS ENGINEERING

The effect of turbulence on the oxygen uptake of water

Author:
Astri Nore

Supervisor:
Jason Hearst

Co-supervisor:
Pim Bullee

10. June, 2022

Abstract

The influence of turbulence on the oxygen transfer rate across an air-water interface is investigated experimentally in a large recirculating open water channel with an active grid to control the turbulent conditions in the flow. Four different turbulence intensities are generated with an active grid, ranging from 2% to 7% with Taylor Reynolds numbers between 15 and 335. The water is initially depleted of dissolved oxygen by adding sodium sulphite that binds with the oxygen in the water. After all the sodium sulphite has reacted, oxygen from the air above the water channel will be taken up by the water until it reaches saturation. A fine optical oxygen probe measured the oxygen concentration, from which the gas transfer rate was obtained. The turbulence conditions are quantified using laser Doppler velocimetry and particle image velocimetry. Surface area variations and surface movements were monitored by a wave probe and synthetic Schlieren setup. There is significant knowledge about the properties of air and water, but less is known about the mechanisms of the gaseous transfer between them. This study investigates how turbulence influences the gas transfer rate by only varying the turbulent conditions. The changes in the surface area and surface roughness for the different turbulent conditions were negligible from the analysis of the data obtained with the wave probe and the synthetic Schlieren setup. The present study revealed that the gas transfer rate increases with higher turbulence intensities. This study indicates the smaller scales appear to impact the gas transfer rate for higher Reynolds number.

Sammendrag

Påvirkningen av turbulens på oksygenoverføringsraten mellom luft og vann undersøkes eksperimentelt. Dette blir gjort i en stor, resirkulerende vannkanal med et aktivt grid for å kontrollere turbulensen. Fire forskjellige turbulensintensiteter genereres med det aktive griddet, fra 2% til 7% med Taylor Reynolds tall mellom 15 og 335. Frie oksygenmolekyler fjernes fra vannet ved å tilsette natriumsulfitt. Når alt natrium- sulfittet har reagert, vil oksygen fra luften bli tatt opp av vannet til det blir mettet. Gassoverføringsraten ble funnet av en oksygenprobe som målte oksygenkonsentrasjonen. Metoden for kvantifiseringen av turbu- lensforholdene var laser Doppler velocimetry og Particle image velocimetry. Bølger og overflatekonturer ble målt av en bølgemåler og et syntetisk Schlieren-oppsett. Oksygenoverføring i et luft-vann-grensesjikt er viktig på mange områder. Eksempler på dette er i industrielle applikasjoner, innsjøer, vannkvalitet, og overføring av gasser i luft-vann-grensesjikt er en viktig del av det globale karbonkretsløpet. Det er mye kunnskap om egenskapene til luft og vann, men mindre kjent er mekanismene for gassoverføringen mel- lom dem. Denne studien undersøker hvordan turbulens påvirker gassoverføringsraten ved kun å variere de turbulente forholdene. Analysen av data fra bølgesonden og det syntetiske Schlieren-oppsettet viste at endringene i overflaten var neglisjerbare. Denne studien viser at gassoverføringsraten øker ved høyere turbulensintensiteter. Denne studien indikerer også at de mindre turbulente skalaene ser ut til å påvirke gassoverføringsraten.

Acknowledgements

Table of Contents

List of Figures

List of Tables

1   Introduction

The mechanism of the gas exchange across an air-water interface is a subject of fundamental importance. Areas where air-water dissolved gas transfer is significant range from water quality (reaeration) to geo-chemical cycling of materials to industrial applications (Herlina and Jirka, 2008). Air-water gas transfer is important in environmental and chemical engineering. The study of gas transfer in for example stirred vessels, open channel flow, two-phase flow and the interaction between the transfer process and chemical reactions is a long-standing research topic (Danckwerts, 1951). There is a considerable amount of know-ledge about the properties of air and water, but less is known about the mechanisms of gaseous transfer between them. This deficiency has become even more apparent in recent years with an increasing concern of the transport of greenhouse gasses, many of whose pathways involve transfer across air-sea interfaces. An enhanced understanding of the air-sea interface gas exchange is crucial since this governs the CO_2 balance (Prentice et al., 2001). As mentioned, another area where the mechanisms of gas exchange across an air-water interface is significant is in natural rivers and aquatic systems. The amount of dissolved oxygen (non-compound oxygen) is essential in assessing water quality, and too high or low dissolved oxygen levels can harm aquatic life. An interest in the gas transfer mechanisms arose from the need to predict the oxygen dynamics in rivers downstream of a pollutant source, such as organic waste. The bio-degradation processes of the organic wastes, which consume oxygen at a very high rate, lead to a DO (dissolved oxygen) deficit in the river (Herlina and Jirka, 2008). To replenish the DO concentration, active reaeration is often used, especially in streams. An essential element of water quality modeling is in-depth knowledge of the gas absorption process to accurately predict the reaeration rate is thus an essential element of water quality modeling.

Two important variables for the gas exchange are the partial pressure difference across the air-water interface and the gas transfer rate, often referred to as the reaeration coefficient, k_L. The partial pressure in the atmosphere gives the corresponding equilibrium concentration in water. Henry's law describes that the equilibrium concentration of the oxygen in the water is proportional to the partial pressure of oxygen in the air. Partial pressure differences are easily obtained from measurements, but the gas transfer velocity remains illusive. This results from challenging experimental investigations and modeling, which does not allow for quantitative comparisons. Direct measurements of the gas transfer across the interface are complex, and therefore, further investigations to enhance knowledge of this topic are crucial. This study focuses on the gas transport on the waterside of an air-water system. The air-side motions have a small effect on the interfacial gas transfer rate because of the greater diffusivity of the gases in air compared with water and the low solubility in water. This gives a homogeneous gas concentration in the air while a concentration boundary layer forms in the water near the interface (Turney and Banerjee, 2013). The advection-diffusion equation describes the concentration field

$$\frac{\partial c}{\partial t} = -\nabla \cdot \mathbf{F}, \tag{1}$$

where c is the concentration and $\mathbf{F}$ is the flux of gas species. The gas transfer process is governed by molecular diffusion and turbulent exchange processes, and the gas flux $\mathbf{F}$ can be written as

$$\mathbf{F} = \mathbf{v}c - D\nabla c, \tag{2}$$

where $\mathbf{v}$ is the fluid velocity and D is the molecular gas diffusivity. The first term on the right-hand side of the equation governs the turbulent mass transport. The second term on the right side represents diffusion. Gas molecules move due to a concentration gradient, from a region of high concentration to another region with lower concentration. This is a passive process, meaning that no energy is required and it is governed by Fick's law (Paul et al., 2014). The instantaneous gas flux across the air-water interface is by diffusion

$$F_i = D\frac{\partial c}{\partial n}|_i, \tag{3}$$

where subscript i denotes a location on the air-water interface and n denotes the normal distance to the interface. Equations 1, 2 and 3 are linear with respect to the concentration, and the time-averaged flux across the interface is subsequently proportional to the bulk fluid. This can be written as

$$\overline{F_i} = k_L(c^* - c) = D\frac{\partial \overline{c}}{\partial n}|_i, \tag{4}$$

where c^* is the equilibrium dissolved gas concentration, c is the dissolved concentration in the water and k_L is the time-averaged gas transfer coefficient. The overbar denotes time or space averaging.

Gas transfer across the air-water interface has been studied for decades, and numerous theoretical models have been proposed. Many previous studies have tried to find a relation between the gas transfer rate and a global flow property, such as the mean velocity, water depth, wave slope, and surface divergence (Thackston and Krenkel, 1969; Plate and Friedrich, 1984; Gulliver and Halverson, 1989; Turney et al., 2005). Others have tried to develop more conceptual models. Lewis and Whitman (1924) introduced the film model. This model assumed a stagnant film on each side of the interface where molecular diffusion is the controlling factor in the transport. This model predicts that the mass transfer rate is proportional to the molecular gas diffusivity. This gives the relation $k_L = D/\delta$, where δ is the thickness of the stagnant film. However, this did not coincide with later experiments as it oversimplified the mechanisms of the transfer process (see for example McCready et al., 1986). A decade later, Higbie (1935) proposed a model based on a surface renewal effect, later known as the penetration model. This model suggests that the turbulence in the bulk region of the fluid would bring up new packets of liquid to the surface, where gas transfer takes place for a specific renewal time T. Danckwerts (1951) further modified Higbie's penetration model by allowing the constant renewal time to follow an exponential probability distribution of surface renewal rate so that $k_L = \sqrt{Dr}$. The renewal models show that k_L is related to the square root of D and the renewal rate, r. Several proposals on how to determine the renewal rate r have been given.

Fortescue and Pearson (1967) proposed that r is determined by the time scale of the largest turbulent eddies. Therefore, the renewal rate r can be estimated by u'/L, where u' is the root mean square turbulent fluctuation and L is the turbulent integral length scale. By using the characteristic turbulent velocity and length scales a renewal rate is given by $k_L = \sqrt{Du'/L}$. Lamont and Scott (1970) and Banerjee et al. (1968) suggested to use the time scale of the smallest eddies. By the small eddies, the renewal rate r could be estimated as $r = \sqrt{\epsilon/\nu}$ by the Kolmogorov scales. Where ϵ is the turbulent energy dissipation rate near the interface, and ν is the kinematic viscosity. This gives $k_L = \sqrt{D}(\epsilon/\nu)^{1/4}$. Theofanous et al. (1976) found that Fortescue and Pearson (1967) experiments were at a low Reynolds number, whereas Banerjee et al. (1968) and Lamont and Scott (1970) had conducted experiments at a higher Reynolds number. Therefore, the mass transfer was governed by large-eddy sizes at low Reynolds numbers and the mass transfer was governed by small-eddy sizes at high Reynolds numbers. The governing problem is the specification of the individual renewal rates, which need a direct measurement for the given turbulent conditions. The turbulent contribution to gas transfer is not sufficiently taken into account, and thus no universal formula exists.

Through years of investigation, several measurement techniques have been used to resolve the air-water interface gas transfer. Previous experimental studies have complex techniques for measuring the gas transfer, requiring complicated and unpractical setups. The gas tracer method, floating chamber method and the delta method are some examples (Copeland and Duffer, 1964; Tsivoglou et al., 1965; McBride and Chapra, 2005). The whole tank method evaluates the reaeration coefficient using the recovery speed from the initial gas-depleted state. This is often used in a laboratory recirculating water channel and is used to investigate the gas transfer rate. This method gives the spatially averaged gas transfer rate, but it does not allow for local gas transfer rate measurements. In recent times new technologies have been used, such as laser-induced fluorescence (LIF). LIF measures the instantaneous concentration field of a fluorescent dye (e.g., Herlina and Jirka, 2008). However, this has a drawback for a big water channel, when problems with fluorescent dye dissolution with a constant concentration in space arise.

The turbulence characteristics generated by grid-stirred systems have been studied extensively (Hopfinger and Toly, 1976; McKenna and McGillis, 2004) and are shown to be suitable for investigations of gas transfer (Brumley and Jirka, 1987; Chu and Jirka, 1992). In a grid-stirred system, the turbulence is generated away from the surface and decays towards the surface. This gives similar turbulence characteristics to the water surface in a flowing stream. Herlina and Jirka (2008) investigated the gas transfer process across an air-water interface with turbulence generated by an oscillating grid by using a combined particle image velocimetry laser-induced fluorescence (PIV-LIF) technique. This allowed for synoptic measurements of the two-dimensional velocity and dissolved gas concentration fields. Herlina and Jirka (2008) found that the surface renewal model with eddies larger than the concentration boundary layer was dominant and held better for low Reynolds numbers and the small-eddy model performed better for high Reynolds numbers. A decade later Herlina and Wissink (2019) conducted direct numerical simulations (DNS) of even higher Reynolds numbers and found the small-eddy model performed best. These findings supported the
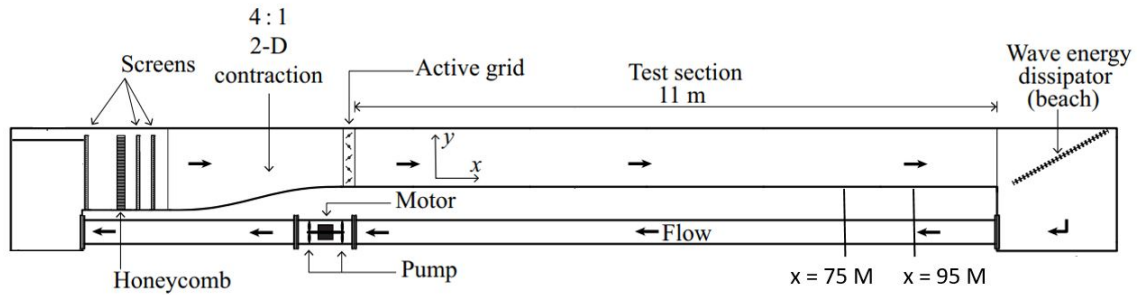
Figure 1: Schematic illustration of the recirculating water channel at the Norwegian University of Science and Technology. PIV was taken at $75M$ and $95M$ downstream of the active grid in the center of the channel. Oxygen measurements, LDV and Schlieren were taken at $95M$ in the channel center. The wave probe was placed 2 cm downstream of the oxygen probe and 15 cm off-center. Positive flow direction is given by the orientation of the x-axis. Adapted from Jooss et al. (2021).

idea of the two distinctive regimes suggested by Theofanous et al. (1976). Sanjou (2020) investigated the local gas transfer rate in different streamwise positions of an accelerated open-channel flow. The CBL (concentration boundary layer) was obtained by traversing the DO probe vertically. The turbulence and gas transfer rate increased from the mid-section of the spacially accelerated region to the end.

In order to investigate the response properties of the gas transfer rate to various turbulence characteristics on a laboratory scale, the large recirculating water channel with an active grid is used. The water is depleted from oxygen by adding sodium sulphite that binds with the dissolved oxygen in the water. When all the salt has reacted the water will start to take up oxygen from the air above it, until it has reached the equilibrium concentration again. The present study measures the streamwise profile of the thickness of the DO concentration layer by a fine needle DO probe at one selected streamwise position of the flow. The concentration boundary layer is obtained by traversing the probe in the wall-normal direction. This is repeated for different turbulence conditions, controlled by the active grid, and quantified using velocity measurements from laser Doppler anemometry, and particle image velocimetry techniques. Many previous studies have proposed models and examined experiments on the bulk gas transfer, but this method allows for the local measurements of the gas transfer rate. Based on previous comparable experiments (Herlina and Wissink, 2019; Sanjou, 2020), the turbulence intensity is expected to affect the gas transfer rate where a higher turbulence intensity gives a higher gas transfer rate.

First, the experimental setup, data acquisition and processing are given in Section 2. Second, the results are presented in Section 3, discussing the effects of turbulence intensity, the different length scales and the free surface deformations on the gas transfer rates. Third and last, the conclusion is given in Section 4.

2   Experimental method

2.1   Facility

The experiments were conducted in the recirculating open water channel at the Norwegian University of Science and Technology (NTNU). The test section measures 1.8 m wide, 0.8 m high, and 11 m long. The facility is designed to study the development and decay of turbulence. The water channel has a 4:1 contraction followed by an active grid upstream of the test section, yielding control of the flow and turbulent conditions in the water channel. A 10 mm thick acrylic plate measuring 1.79 m wide and 1.045 m long was placed at the start of the test section on the water surface to dampen surface waves and air entrainment caused by the active grid itself. The remaining 10 m of the water channel test section had a free surface. The contraction and end sections' water surfaces were covered with a floating plastic film to avoid air-water gas transfer in other areas than in the test section. The water channel has full optical access, making it suitable for optical measurements. The floor of the water channel is smooth and leveled. The water depth was held constant at 17 cm in all experiments. A schematic illustration of the water channel and experimental setup can be seen in Fig. 1.

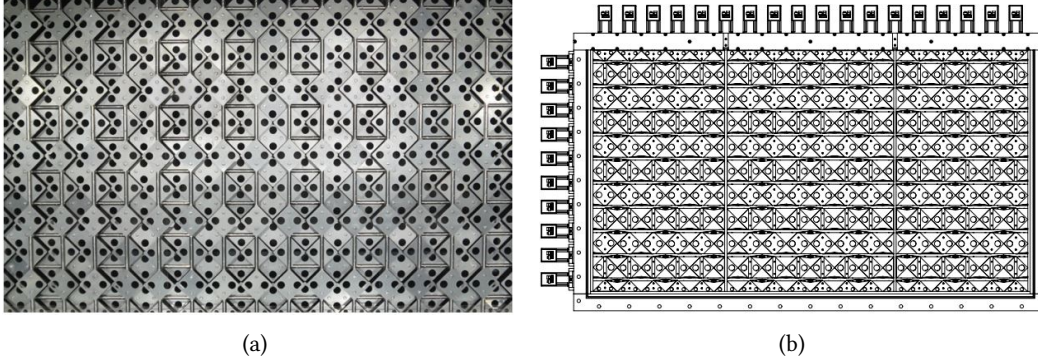<div align="center">(a)   (b)</div>

Figure 2: The active grid with diamond-shaped wings with holes. Viewed from the test section at full blockage (Jooss et al., 2021).

To control the turbulent conditions in the flow, an active grid is used. The active grid used in this study is based on the design of Makita (1991). The active grid consists of 10 horizontal and 18 vertical rods with a diameter of 12 mm. See Fig. 2 for reference. As the water level in this study is 17 cm, only one horizontal rod was used. The mesh length, M, is defined by the center-to-center spacing between each rod and is 100 mm. The width of the active grid spans the entire cross-sectional area of the test section. See Fig. 1 for reference. The rods are equipped with diamond-shaped wings with sides of 70.71 mm and, therefore, a diagonal of 100 mm. The wings have two holes of 24 mm to reduce the motor loading during actuation sequences to avoid complete blockage of the flow. A stepper motor controls each rod independently. The motors have unique ASCII names and control commands are generated and transmitted through MATLAB scripts. The motors can independently control the rotational speed, acceleration and direction of each rod.

2.2 Test cases

Four different flow conditions were investigated in this study. Parameters for the different cases are presented in Table 1. The different experiments will be referred to by their letter in the first column. The mean velocity and turbulence intensity were obtained by LDV measurements close to the free surface. The mean velocity close to the free surface was kept at a constant of $U = 0.41 \pm 0.01 \text{ m s}^{-1}$ for all test cases. The differences in mean velocity are considered negligible. The parameter of interest that varied between the cases was the state of operation of the active grid, which gives different turbulence intensities, u'/U where u' is the root-mean-square of the fluctuating velocities. The reference case, REF, was conducted without the active grid installed. This resulted in a background turbulence intensity of 2.68 % at $95M$. The background turbulence in a water channel flow is typically 2–3 % (e.g. Laskari et al., 2018). Case A was created by keeping the active grid as open as possible, i.e. orienting all the wings parallel with the flow. For the last two cases, B and C, the rods were actuated differently to achieve higher turbulence intensity. For experiments with the active grid, both the horizontal and vertical bars were actuated. The actuation mode for cases B and C was fully random, meaning that the rotational velocity, period and acceleration were varied randomly over a range. The mean rotational velocity Ω varied randomly within a specified value within a top hat distribution ω. The chosen parameters were based on findings from previous experiments (Jooss et al., 2021). The result of this gave a range of turbulence intensities between 2–7% and Re_M around 36–38×10^3. The mesh Reynolds number is defined as $Re_M = UM/\nu$, where $\nu = 1.0034 \times 10^{-6}$ is the viscosity of the water.

2.3 Data acquisition

2.3.1 Dissolved oxygen measurements with a fine probe and vertical traverse

The oxygen in the water was obtained through a 0.8 mm thick extra-fine optical probe, PreSens Microx 4. This oxygen profiling microsensor has a splashproof metal housing around the fiber construction which has a tip that can be extended with a turning mechanism. The measuring range goes from 0–100% O_2.

Table 1: Parameters of the cases at $x = 95M$. Ω is the mean velocity and ω is the top hat distribution. U is the mean velocity, u'/U_{LDV} is the turbulence intensity and Re_M is the mesh Reynolds number obtained from the LDV data. These symbols and colors are used in all figures. For $x = 75M$ the symbols and color scheme is the same except the colors are faded, this can be seen in Table 2.

Test case		$\Omega \pm \omega$	U	u'/U_{LDV}	Re_M ($\times 10^3$)	Symbol
		[Hz]	[m s^{-1}]	[%]		
REF	No grid	-	0.41	2.68	36	●
A	Static grid	-	0.41	2.86	36	■
B	Active grid	0.5 ± 0.25	0.41	4.76	36	◆
C	Active grid	0.05 ± 0.025	0.42	7.25	38	▼

This measurement technique is advantageous for this experiment because of its small size, and it can be assumed that it has a negligible impact on the flow (Sanjou, 2020). The probe signal does not depend on the flow rate and has a maximum sampling rate of 1 Hz. The probes allow for measurements with high spatial resolution, and there is no use of a reference electrode. This makes the optical probe eligible for low flow velocities compared to classical electrode type probes. The probe has a response time of 10 seconds in liquids and an accuracy of ± 0.05 % O_2. The microsensor calibration is performed using a conventional two-point calibration in oxygen-free water (Cal0) and air-saturated water (Cal100). Several conditions can affect the preciseness of the measurements. To avoid inaccurate measurements temperature compensation is used. Assuming a uniform temperature distribution, a thermocouple temperature sensor was placed downstream of the oxygen sensor at $110M$ in the settling tank to not disturb the free surface in the test section of the water channel. Unexpected gradients or drifts can also occur if the optical fibre tip is not entirely extended or air bubbles are on the sensor tip. Continuous illumination of the sensor tip over 24 hours may lead to a phase drift towards a higher concentration. The microsensor is connected to an oxygen meter, OXY-4 ST. The oxygen meter is operated with PreSens Measurement Studio 2 software which enables control of the device (Wallingford, 2021).

In this study, the oxygen probe was installed $95M$ downstream of the active grid (See Fig. 1 for reference). In order to spatially resolve the concentration boundary layer (CBL), the oxygen sampling was done at various heights by traversing the probe up and down. The traverse has a maximum velocity of 5.8×10^-3 m s^{-1} and an accuracy of $1\,\mu$m. To avoid hysteresis, the first measurement point was always reached from the same reference location. An important factor while determining these measurement positions was to have small enough steps in the near-surface region to get a clear view of the CBL. As the depth of the water channel was determined by visual inspection by measuring 17 centimeters in the test section, some inaccuracies were expected. Therefore, the surface was also found iteratively and accounted for in the oxygen probe traversing code. This was done by traversing the probe up and down in small steps in still water in the water channel until the point right above the surface was identified from disturbances of the free surface. Wave probe measurements were also taken to ensure the correct water depth in the test section while the water was running. This procedure is described further in Section 2.3.3. The traverse moved to a new position every 60 s. To ensure the stability of the measurements, the first 15 seconds of the oxygen measurement for each traversing position were removed due to the response time of 10 s. In addition to this, the 10 last seconds of the measurement were removed; therefore, there were 35 point measurements left in each traversing position with a sampling rate of 1 s^{-1}.

2.3.2 Laser Doppler velocimetry (LDV)

Parts of this subsection are adapted from previous project work of the author with some modifications and additions (Nore, 2021). The streamwise and transverse velocity components were measured with laser Doppler velocimetry (LDV). LDV has been applied extensively to characterise fluid flows. The high spatial resolution and its ability to resolve rapid fluctuations makes it a suitable tool for studying turbulence (Doran, 2013). The LDV working principle is using the Doppler shift effect. A Doppler shift is a common phenomenon and can be experienced in everyday life, such as when the pitch changes as a siren moves
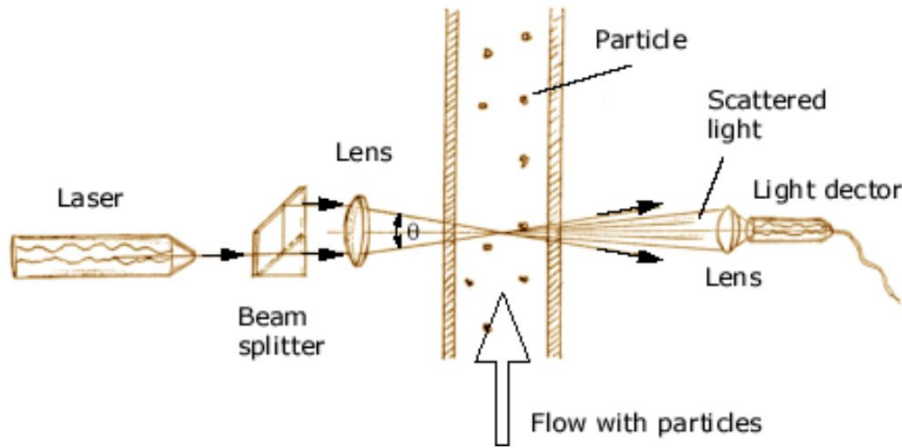
Figure 3: A flow is seeded with particles that scatter light. The laser beams hit a particle that reflects a scattered light which is collected by a detector. By the Doppler shift, the frequency of the laser beams and therefore the velocity of the fluid particle can be determined. Figure from Doda (2008).

away or towards you. The same effect also applies to light. LDV is a widespread technique for point wise velocity measurements of fluid flows, which uses this concept. The water channel is seeded with small, neutrally buoyant, passive particles. When the laser beam with known frequency hits the moving particles, the light is scattered and its frequency is received by a stationary detector. In this way, it invokes the Doppler shift twice. The Doppler shift is directly proportional to the frequencies and to the velocity of the particles (Ikeda et al., 1994; Tropea et al., 2007). Figure 3 illustrates the concept of LDV. LDV depends on particles in the flow that follow the flow's velocity and fluctuations. The sampling rate of the LDV measurements varies with the velocity of the particles and the sampling rate is therefore non-constant. As the LDV is not measuring the flow, but the particles in the flow, it is essential to select the right particles. They should be small and light enough to follow the flow and not fall down on the floor in the water channel. Simultaneously, they should also be big enough to scatter the light significantly. Correct selection of particles increases the data signal and simultaneously gives a higher measurement accuracy. For LDV small particles are preferred, but larger particles can be used as long as they are buoyancy neutral.

The particles used in this experiment were purchased from Microbeads AS, and are Dynoseeds TS40 6317. The seeding has a mean diameter of $43.5\,\mu$m, density of 1050 kg m^{-3} and a standard deviation in their size of $0.87\,\mu$m. The LDV was taken $95M$ downstream of the active grid and was used to obtain velocities and to investigate the turbulence intensity. The LDV was used to determine the turbulence characteristics of the different active grid sequences and the necessary motor power to keep the velocity constant. As the objective of the project is to investigate the effect of turbulence on the gas transfer rate of the water side of an air-water interface, a variety of turbulence intensities was desired. When the correct velocity was found (0.4 ms^{-1}) for a grid setting, a measurement was taken (240 s) and the turbulence intensity was obtained. After taking several measurements, and evaluating how much time each experiment would take, two of the different active grid settings were chosen for further investigation. This is presented in Table 1.

As mentioned, LDV has a non-uniform time series, and it is therefore necessary to resample the data to do spectral analysis. This was done by the sample and hold method as described by Adrian and Yao (1986) and Boyer and Searby (1986). By use of this method, a uniformly spaced time series is obtained. The data rate varies for the streamwise and transverse velocity components, and therefore different resampling frequencies were used. The data rate for the streamwise and transverse velocity was approximately 200 Hz and 100 Hz for the most turbulent case, accordingly. This was resampled to 250 and 150 Hz.

2.3.3 Wave probe

In this study, a wave probe was installed $95M$ downstream of the active grid, next to the DO probe in the test section to measure the amplitude of the waves in the water channel (See Fig. 1 for reference).
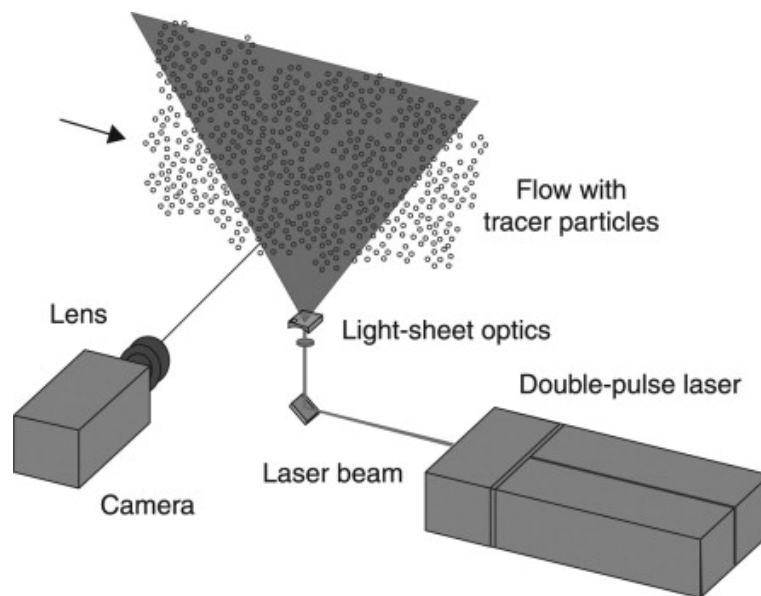
Figure 4: Schematic illustration of how PIV works. The flow with tracer particles is illuminated by a light sheet and is captured by the camera. Figure from Lindken and Burgmann (2012).

The wave probe is an Ethernet Wave Probe system created by HR Wallingford (Wallingford, 2021). The wave probe monitor measures the electrical current flowing between immersed, stainless steel probes. This current is proportional to the depth of immersion and can be calibrated by varying the immersion depth. The calibration was done by changing the immersion and manually registering the changes. The wave probe is equipped with a calibration stem with positioning holes to do this accurately. The wave probe has an accuracy of ± 0.1 mm. In order to acquire and analyze the data, HR DAQ (Data acquisition and analysis software) was used, this is especially suitable for wave probes. HR DAQ gives a real-time display of the required data and a calibration routine.

The wave probe was used to ensure correct water depth. The wave probe was calibrated in the water channel with 17 cm depth of water and no flow. When the water channel was turned on with the different active grid settings, a hydraulic jump naturally occurred as well as a more wavy surface in the test section. Therefore, the water level dropped and the channel had to be filled further in order to have 17 cm in the test section while the water was flowing. As this is difficult to view optically, short measurements were taken with the waveprobe. By taking a 120 seconds measurement in still water and comparing it to a similar measurement of flowing water, the head loss was obtained and the water level could in that way be measured and corrected. However, it was difficult to get exactly 17 cm height, and therefore, the head loss was implemented in the surface position in the MATLAB traversing script.

2.3.4 Particle image velocimetry (PIV)

As most common fluids are transparent and therefore the fluid motion is not easy to view, techniques to record the motion are necessary. During the past decades the development of digital cameras and processing technology has resulted in quite succesful methods, such as PIV (Tropea et al., 2007). PIV is an optical field technique used to measure instantaneous velocity distributions in a plane of the flow (Cengel and Cimbala, 2013). Tracer particles are injected into the flow and are small enough to follow the fluid motion. The tracer particles are then illuminated by a light sheet generated from a pulsed light source so that the particles are visible. The light scattered by the particles is recorded in two subsequent image frames by a digital imaging device. The motion of the particles is used to calculate the speed and direction of the flow. Compared to other measuring techniques such as LDV, PIV can produce vector fields. PIV is a non-intrusive method, but requires optical access for the delivery of the light sheet and recording of images. In order to get a representative image, the tracer particles must be homogeneously spread out in the flow. Figure 4 illustrates the concept of PIV.

For the PIV measurements a 25 megapixel camera was used (Imager MX 25M), combined with a 100 mm

macro lens (ZEISS Milvus 100M). The camera was mounted on one side of the water channel in the center of the width at $75M$ and $95M$ downstream of the active grid. A Litron Nano L200-15 laser, which is a Nd-YAG dual-pulse laser with a measured power of 208 mJ per pulse was used to illuminate the particles. The particles used were the same as for the LDV. In each measurement 2000 independent image pairs were acquired by the camera. The sampling rate was 2 Hz and the time between the two subsequent frames was $1125\,\mu$s.

LaVision DaVis 10 was used to collect and process the data. The minimum value of every pixel in the entire data set was subtracted to decrease background noise and a Gaussian profile was used to generate the sliding average across five pixels. To adjust for orthogonality, image correction was used. For the initial pass, the processing was done with a window size of 96×96 pixels with a 50% overlap. The final window size was 48x48 pixels with a 50% overlap. There were 128×128 vectors in the raw uncropped vector field. The spatial resolution of the PIV is approximately 0.180m and the vector spacing is around 0.8 mm.

2.3.5 Synthetic Schlieren

Synthetic Schlieren in an optical method to measure the instantaneous topography of the interface between two transparent fluids. The different active grid settings generates turbulence and waves which results in a different free surface area. The measurement of the deformation of the water surface is important to get insight into the different surface areas as this affects the gas transfer rate. Non-intrusive, optical methods are of much interest as it is of crucial importance to not disturb the flow. The method used in this experiment is adapted from Moisy et al. (2009). The method is based on analyzing the refracted image of a random dot pattern visualized through the air-water interface of the water channel. The random dot pattern is placed above the water surface with a camera placed directly below it under the water channel. The displacement field between the refracted image with waves and a reference image is obtained using a digital image correlation (DIC) algorithm. Numerical integration of this displacement field based on a least-square inversion of the gradient operator is used to reconstruct the instantaneous surface height. This gives excellent spatial resolution with low computational cost. For the synthetic Schlieren measurements a Photron Fastcam Mini WX100 camera was used, combined with a Sigma 105 mm macro lens. The camera was under the water channel in the center of the width at $95M$ downstream of the active grid. Three independent imaging sequences were taken for each case to achieve statistically independent results. In one imaging sequence, 1500 images were taken with a frequency of 50 Hz.

The relative uncertainty of the surface height reconstruction is expected to depend linearly on the uncertainty ϵ_e of the input displacement field. This value, $\epsilon_e = 0.035$, was found by performing an auto correlation in DaVis, where the distance from peak to peak is used. The uncertainty calculated by DaVis was calculated over 50 of images for all vector fields of C. As this is the most turbulent case, it was also expected for it to have biggest surface deformation and therefore highest error. This will be elaborated on further down in the section. Furthermore, the uncertainty had high local peaks but as the mean uncertainty was low, it was deemed sufficient. From Moisy et al. (2009), the resolution of the surface reconstruction is

$$\frac{\Delta\eta}{\eta_{rms}} \cong 5\frac{L_e}{\lambda_e}\frac{\epsilon_e}{N}, \tag{5}$$

where η is the amplitude, $L_e = 16.5$ cm is the length of the field, $\lambda_e = 16.5$ cm is the wavelength, $N = 128$ is the number of mesh in a window. This gives an uncertainty of 1.5×10^{-3}. A wave with amplitude of 1 mm should be measurable with a precision of 1 µm. Moisy et al. (2009) underline that the estimate given in Eq. 5 should be considered as the lowest bound for the uncertainty. The displacement field noise, ϵ_e could be bigger than DaVis is able to estimate, when large strains are present. This makes it impossible for DaVis to resolve it. However, this happens when there is large curvature in the surface, and is not a threat for the small surface movements seen in this study.
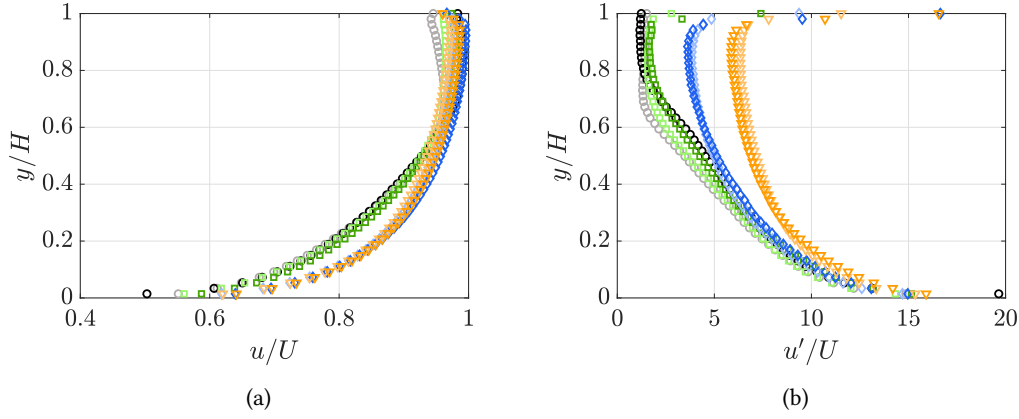
(a)   (b)

Figure 5: Velocity profiles for REF ●, black; A ■, green; B ◆, blue; C ▽, orange at $95M$ with faded colours at $75M$. The figures display the (a) streamwise mean velocity profile and the (b) turbulence intensity for the streamwise velocity. The depth is normalized by the depth of the water level, $H = 17$ cm. Only every third data point is plotted to achieve more clarity.

3   Results and discussion

3.1   Flow properties

Four different inflow conditions were investigated throughout this study. The streamwise velocity profiles for all cases obtained by PIV and normalized by the mean velocity close to the free surface are presented in Fig. 5 (a). The y-axis is the wall normal depth normalized by the water height, H=17 cm. It should be noted that the figures in this section have one colour and marker for each case, with a lighter shade for the quantities obtained at $75M$ and a darker shade at $95M$. Symbols are presented in Table 2. Figure 5 (a) indicates the boundary layer is fully developed for all cases at $95M$ as the profiles do not deviate significantly from $75M$. The oxygen measurements were conducted at $95M$ and hence the trends at this position will be discussed. In addition, the vertical position where the oxygen probe was submerged in the bulk is interesting to investigate as this is where the gas transfer coefficient is computed. Therefore, the values reported in Table 2 are given at this depth, namely $y/H = 0.95$. Profiles of the turbulence intensity obtained from the PIV data are given in Fig. 5 (b). The turbulence intensity is higher closer to the free surface. Figure 5 (b) displays that the turbulence intensity is quite similar for the downstream positions for each case, but lower at $95M$ compared to $75M$. Table 2 additionally includes the turbulence intensity obtained by the LDV, u'/U_{LDV}. These are higher than the results obtained by the PIV, as the LDV was taken even closer to the free surface.

The streamwise spatial correlation is calculated to estimate the scales of the flow. The LDV data is sampled infrequently, and the data post-processing method with sample and hold creates artificial points to get a constant time stamp. This will bias the correlation function, and therefore the PIV data was used. The correlation coefficient between two quantities, A and B, is defined as

$$R_{AB} = \frac{\overline{A(x,y)B(x+\Delta x, y+\Delta y)}}{\sigma_A \sigma_B}, \tag{6}$$

where Δx and Δy denote the streamwise and wall normal spacing (Dogan et al., 2019). In this study, only the streamwise correlation is calculated for the streamwise- and wall normal components of the instantaneous velocity fields. The overline denotes the ensemble average. Velocity correlations are computed at all wall normal positions for the each locations of all frames and normalized with the variance. Figure 6 (a) shows the autocorrelation R_{uu} for the streamwise velocity fluctuations computed at different streamwise locations for all cases. Figure 6 (b) shows the same for the transverse velocity fluctuations. The autocorrelation for each case displays the same tendencies and follows the same curve. The variation between R_{uu} and R_{vv} display the same tendencies as Dogan et al. (2019), where R_{vv} have slightly higher negative values and a sharper peak. Sharpness in the peak indicates lower correlations of the transverse velocity fluctuations in the streamwise direction.
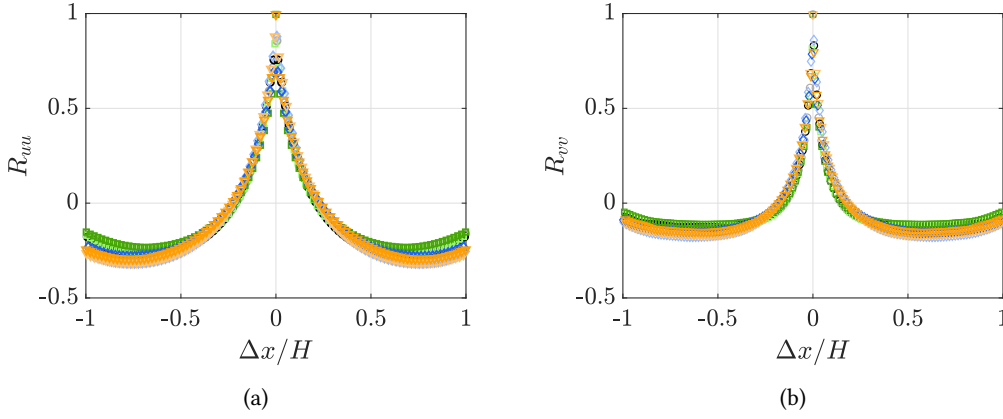
Figure 6: Autocorrelation for REF ●, black; A ■, green; B ◆, blue; C ▼, orange at $95M$ with faded colours at $75M$ at $y/H = 0.95$. Only every third data point is plotted for clarity. Figure (a) is the autocorrelation R_{uu} and figure (b) is the autocorrelation R_{vv}.

Two different estimations of the integral length scale based on R_{uu} and R_{vv} were performed in this study. The first method to estimate the integral length scales is done by integrating R_{uu} and R_{vv} up to the first zero-crossing (O'Neill et al., 2004). The integral length scales estimated by this method are denoted $L_{x,uu,A}$ or $L_{x,vv,A}$. The subscript uu means it is based on the streamwise autocorrelation. In addition to this, length scales at each height were also estimated from R_{uu} and R_{vv} as previously done by Dogan et al. (2019) and Christensen and Wu (2005). Here, the typical length scale of the correlation is defined as twice the length, $L_{x,uu,dx} = 2\Delta x$ where $R_{uu} = 0.5$. The estimated length scales are presented in Figure 7, showing streamwise averages for all wall-normal positions.

Figure 7 (a) and (b) display the same trends, but differ from each other whereas $L_{x,uu,dx}$ have somewhat more extreme values compared to $L_{x,uu,A}$. Figure 7 (b) also display more steps or plateaus. The steps are a result of Δ x being a constant value for the different heights. Because $L_{x,uu,dx}$ only uses one point for the calculations, it is less susceptible to variations compared to $L_{x,uu,A}$. In the bottom half of the channel, i.e., $y/H < 0.5$, the length scale is longer at $75M$ than $95M$. At $75M$, the length scales are quite similar for all cases. At $95M$ there is a bigger variation between the cases, with the largest deviation from $75M$ to $95M$ for A. Closer to the free surface, there is a change in the trends. Case B and C have the largest length scales, followed by REF and then A. B and C follow quite closely, whereas A and REF have the lowest values. The variation between the length scales increases closer to the free surface, and the difference between B and C versus A and REF increases. This indicates that B and C are more dominated by larger scales in the free surface region. Figure 7 shows similarities between the two different estimated length scales in (c) and (d), but again with somewhat more extreme values in (d). Figure 7 (c) and (d) show an even bigger deviation between REF and A versus B and C closer to the free surface, where the length scale for B and C grows noteworthy bigger. Figure 7 displays that $L_{x,uu,A}$ and $L_{x,uu,dx}$ have a steeper curve and obtains higher values of the length scales at grater depths compared to $L_{x,vv}$. A collection of the length scales at $y/H = 0.95$ is given in Table 2. The results indicate a smaller length scale for a lower turbulence intensity, which agrees with the results reported in Dogan et al. (2019), who used $L_{x,uu,dx} = 2\Delta x$ for $R_{uu} = 0.5$. It should be noted that the integral length scales and the other turbulent parameters are estimated from local measurements. The oxygen uptake is affected by a process that happens throughout the entire test section where the conditions in the flow vary with the downstream position, and the turbulence decays. Figure 7 displays this, showing a difference in the estimated scales at $75M$ and $95M$. The macro Reynolds number Re_L based on the integral length scale $L_{x,uu,A}$ is also calculated and presented in Table 2.

The turbulence energy dissipation rate is calculated from the spatial gradient of the streamwise velocity fluctuations as $\epsilon = 15\nu\langle(\partial u/\partial x)^2\rangle$. A fifth-order central differencing scheme was used to determine the gradients. As mentioned in Section 2.3.4, the spatial resolution of the PIV is around 0.8 mm and could create a bias for low values for ϵ. The sampling frequency of the LDV is also too low to fully resolve the flow. This bias also applies for other parameters which are based on the spatial gradient of the streamwise velocity fluctuations, such as λ, Re_λ and η. All of these parameters will be elaborated upon in this section.
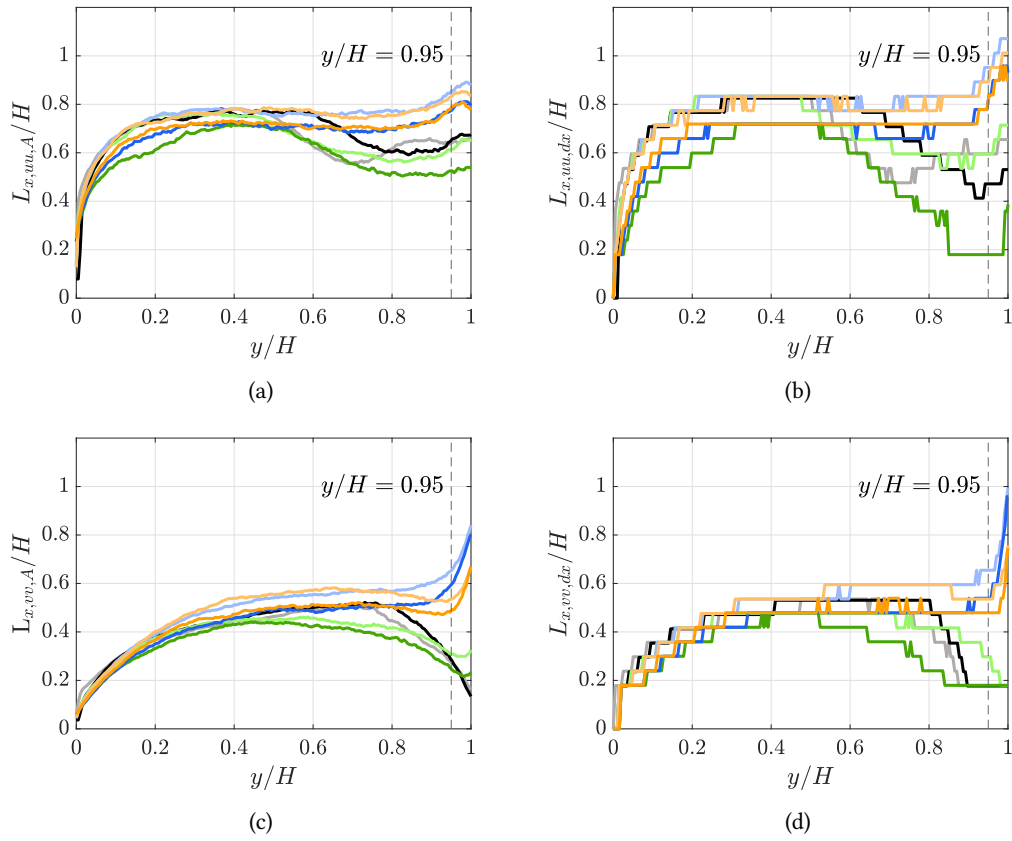
Figure 7: Integral length scale estimates for REF ●, black; A ■, green; B ◆, blue; C ▼, orange at $95M$ with faded colours at $75M$.
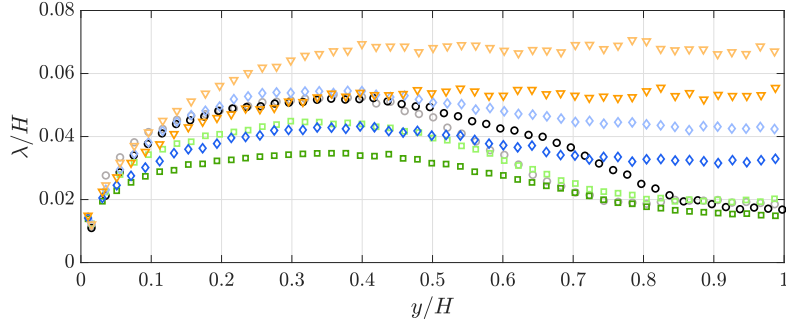
Figure 8: Estimation of Taylor microscale for REF ●, black; A ■, green; B ◆, blue; C ▼, orange at $95M$ with faded colours at $75M$ versus wall normal position, only every fourth data point is plotted for clarity.
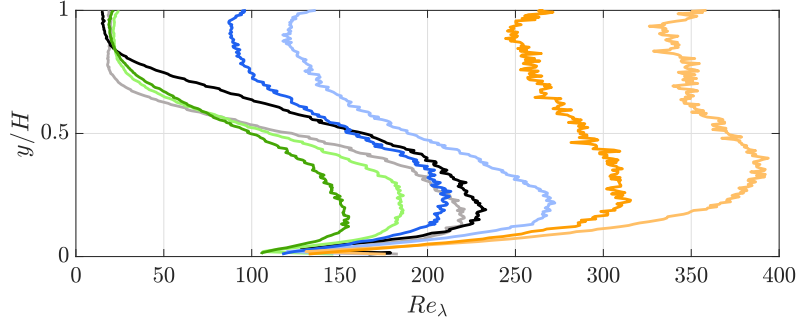

Figure 9: Estimation of the turbulence Reynolds number for all cases at all wall normal-positions. REF ●, black; A ■, green; B ◆, blue; C ▼, orange at $95M$ with faded colours at $75M$.

The Taylor microscale was estimated as

$$\lambda^2 = \frac{2u'^2}{\langle(\partial u/\partial x)^2\rangle}, \tag{7}$$

and is shown in Fig. 8 for each wall normal position. Figure 8 displays that the Taylor microscale decreases farther downstream of the grid for each case. Except from REF, the Taylor microscale also grows with a growing turbulence intensity, where the variations are most significant closer to the free surface. Closer to the free surface, the variations in each case increase at the downstream positions for B and C, but for REF and A the λ collapse.

The different turbulent conditions are characterised by its Taylor Reynolds number based on the Taylor microscale

$$Re_\lambda = \frac{u'\lambda}{\nu}. \tag{8}$$

The Taylor Reynolds numbers Re_λ were calculated to be between 15 and 335, which is presented at $y/H = 0.95$ in Table 2. Re_λ is presented for each wall normal position in Fig. 9. The Taylor Reynolds number displays a trend that decreases farther downstream of the active grid and grows with the growing turbulence intensity. The figure shows that λ is approximately equal for REF and A, while B and C are higher in the near-surface region. Figure 9 indicates the turbulence decrease Re_λ in the boundary layer, but increase or stabilise towards the free surface. In the boundary layer there is a turbulence production of shear, as seen near the wall in Fig. 9. The other source of turbulence in this study, is the active grid turbulence. This decays downstream of the grid, and therefore the Taylor Reynolds number is lower when $y/H > 0.5$. The Kolmogorov length scale, $\eta = (\nu^3/\epsilon)^{1/4}$, is also presented in Table 2. It should be noted that it is not resolved; they are provided here only for a relative reference. The global anisotropy, u'/v', is given in Table 2. The typically reported anisotropy is between 1.1 and 1.2 for grid turbulence. The values in Table 2 are therefore a bit higher than what is usually presented (such as Lavoie et al., 2007), but also lower than the anisotropy in other grid studies (Dogan et al., 2019). As reported by Hearst and Lavoie (2015) an increase in turbulence intensity by an active grid results in loss of isotropy.
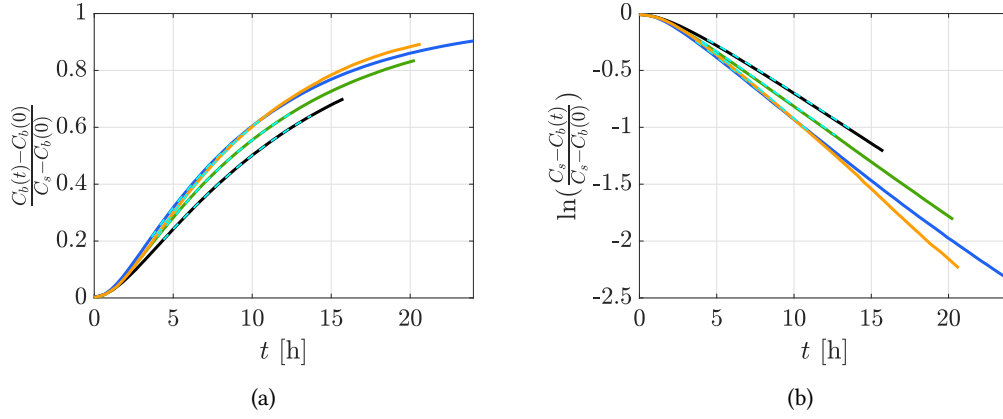
Figure 10: Time variation in the dissolved oxygen concentration in the bulk layer normalized by an initial value $C_b(0)$ and a saturated value C_s for REF ●, black; A ■, green; B ◆, blue; C ▼, orange at $95M$. The linear reduction region for each case is marked with a dashed cyan line. The figures displays (a) linear plot (b) semi-logarithmic plot.

3.2 Oxygen measurements

In this study, water was initially depleted from oxygen by adding sodium sulphite to the water channel. After this, the oxygen from the air reacts with the sodium sulphite until the water becomes saturated. The oxygen concentration was measured using a Presens Microx 4 fine optical probe. Figure 10 (a) shows the normalized linear time series of the oxygen concentration in the bulk. The absolute oxygen concentration in the bulk C_b and at the surface C_s tend to differ slightly for the different experiments. Therefore, the results are presented in a non-dimensional and normalized form. The oxygen concentration is normalized by the mean of the measurements from the initial bulk concentration and the saturated concentration. The saturated concentration is obtained from the oxygen measurements above the surface throughout the time series. The initial start time for each of the time series, $t = 0$, is determined by where the gradient of the gas concentration slope is larger than 0.001 s^{-1}. This was deemed sufficient by performing a sensitivity analysis to get the highest gradient possible while retaining a value close to the surrounding values. Figure 10 (a) shows that there is a variation in the gas transfer rate where REF is the slowest, A is faster and B and C are the fastest and appears to be quite similar. This will be discussed further in the next section. As can be seen from Fig. 10 (a), the cases were not measured for the same duration. For example, REF lasted approximately 16 hours while B lasted for more than 25 hours. Only the smallest time period of REF will be used for all cases to achieve the same time span. Initial tests revealed that it was sufficient to evaluate the gas transfer rate from the shortest time span, REF.

The gas transfer rate is determined through the time measurement of the oxygen concentration. The procedure of finding the gas transfer rate obtained with the DO measurements is as described in Herlina and Jirka (2008). The total gas transfer can be modeled by the conservation of mass equation

$$\frac{dC_b}{dt} = k_L/H\Delta C, \tag{9}$$

where the left hand side is the gas transfer flux, k_L is the gas transfer convection velocity and $\Delta C = C_s - C_b$. By integrating the equation above with initial conditions $(C_s - C_b)_0$ at $t = t_0$ yields,

$$\ln(C_s - C_b)_0 - \ln(C_s - C_b) = \frac{k_L}{H}(t - t_0) \tag{10}$$

where H is the water depth. In the literature, k_L/H is often referred to as the reaeration coefficient k_2. The reaeration coefficient k_2 and convection velocity k_L are obtained through DO time-decay. By plotting the measured oxygen concentration time series at the form of Eq. 10 as in Fig. 10 (b), evaluation of the slope in the linear reduction region gives the reaeration coefficient, k_2. This region is marked with a cyan stapled line in Fig. 10. It is worth mentioning that k_L and k_2 are global values, meaning it applies for the entire water channel and is constant in the linear reduction stage. As a result, the linear reduction region

Table 2: Boundary layer parameters, gas transfer rates and surface area parameters of the test cases at the different streamwise positions. The symbols provided are used in all figures in this section for the different cases.

Test case	x/M	u'/U_{LDV} [%]	u'/U [%]	$L_{x,uu,A}$ [m]	$L_{x,uu,dx}$ [m]	$Re_L(\times 10^5)$	$\epsilon\,(\times 10^{-5})$ [m]	u'/v' [m]	Symbol
REF	75		1.4	0.10	0.10	11	14	1.3	⬤ (grey)
	95	2.68	1.2	0.10	0.07	9	12	1.3	⬤ (black)
A	75		1.7	0.10	0.10	14	13	1.2	◼ (light green)
	95	2.86	1.8	0.08	0.03	12	26	1.2	◼ (green)
B	75		4.1	0.14	0.16	47	19	1.3	◆ (light blue)
	95	4.76	3.9	0.13	0.13	41	29	1.3	◆ (blue)
C	75		6.5	0.14	0.15	74	23	1.5	▼ (light orange)
	95	7.25	6.1	0.13	0.13	65	32	1.5	▼ (orange)

case	x/M	u'/U_{LDV}	$\eta\,(\times 10^{-4})$ [m]	λ [m]	Re_λ	$k_2\,(\times 10^{-6})$ [s^{-1}]	$k_L\,(\times 10^{-3})$ [cm s^{-1}]	δ_{CBL} [mm]	γ [%]	$\langle S^2 \rangle$ [%]
REF	75		3.1	0.0032	19.7					
	95	2.68	3.1	0.0029	15.6	37	0.63	4	0	0.00002
A	75		3.0	0.0033	21.8					
A	95	2.86	2.6	0.0026	19.1	40	0.68	5	0.02	0.0008
B	75		2.8	0.0072	121.5					
B	95	4.76	2.5	0.0055	88.1	49	0.83	-	0.17	0.0054
C	75		2.6	0.0113	334.8					
C	95	7.25	2.4	0.0090	249.5	52	0.88	8	0.16	0.0053

is the most interesting because it is straightforward to compare for different cases. Normalized oxygen concentration values between 0.2 and 0.6 were used to calculate the gas transfer coefficients, to ensure it was evaluated within the linear reduction region for each case. Table 2 displays k_L and k_2 for all cases. It should be noted that when k or is referred to in this study, it is referred to both k_L and k_2 as they are proportional and display the same trends.

The obtained values of k correspond to Fig. 10 - the gas transfer coefficients appear to increase in the order REF, A, B and C. From Table 2 it is possible to see that k increases when more turbulence is added. From REF to A, there is a slight increase in k, as well as in the turbulence intensity. There is a larger increase in k from REF to B, and a significant increase in the turbulence intensity. The same is seen from REF to C, where the turbulence intensity significantly increases from REF and the gas transfer rate has also increased. This is intuitive as turbulence gives more mixing to the flow and, therefore, a higher gas transfer rate. Figure 11 (a) display k_L plotted against u'. Furthermore, it is interesting to investigate the scales of the turbulent flow to see if any trends could be the reason for the gas transfer rate variations. As can be seen in Table 2, from REF to A there is a decrease in the integral length scale, this could be due to the insertion of the active grid. Therefore, it is more reasonable to compare B and C to A, and not REF. There is an increase in the integral length scale from A to B, and there is also a great increase in k. The integral length scale is also approximately the same for B and C. This could indicate that the larger scales do not influence the gas transfer rate substantially. The Taylor microscale has the same tendencies as the

integral length scales for REF and A, whereas it decreases somewhat. The insertion of the grid could again explain this. From A to B there is a rather large increase in λ, as mentioned previously also seen in k. There is also an increase in λ from B to C, which is reflected in the k. It could mean that the increase in k is given by the increase in λ as L is the same for B and C. These trends are also in the Taylor Reynolds number Re_λ. Similar reasoning follows for the macro Reynolds number Re_L based on the integral length scale $L_{x,uu,A}$, this is presented in Fig. 11 (b).

The results of the length scales could indicate that the gas transfer rate is more influenced by the smaller scales for this order of Re_L. The same tendency as seen in Fig. 17 with a rise in the low wave number energy for B and C versus REF and A is reflected in the increasing gas transfer coefficient. A possible reason for this could be that the smaller structures govern the gas transfer rate for the higher macroscale Reynolds numbers and the larger scales are more important for the lower macroscale Reynolds numbers. This could be why REF and A almost have the same turbulence intensity but a similar variation in the gas transfer rate as B and C, which have relatively higher turbulence intensity increases between each other. This is supported by Theofanous et al. (1976), Jähne et al. (1987) and Herlina and Jirka (2008) where they present that for low turbulence Reynolds numbers, the larger eddies dominate the influence of the gas transfer rate and for high Reynolds numbers the smaller eddies dominate. It must be noted that the macroscale Reynolds numbers in this study are 2 orders of magnitude larger than Herlina and Jirka (2008), i.e., all measurements in this study are in the high Reynolds regime.

This study only obtained values of k_L for four different turbulent cases, so it is difficult to predict or specify any trends. To investigate whether the gas transfer properties coincide with the proposed models, k_L is compared with the small-eddy model ($k_L = \sqrt{D}(\epsilon/\nu)^{1/4}$) and large-eddy model ($k_L = \sqrt{Du_L/L}$). The molecular diffusivity is approximated to be $D = 1.8 \times 10^{-9}$ m^2 s^{-1} (Castro and Vanderwel, 2021). Figure 11 (c) displays the result of the small-eddy model, and (d) shows the result of the large-eddy model. The figures indicate that the small-eddy and large-eddy models are insufficient to predict the gas transfer rate as both models underestimate it. However, the small-eddy model better reflects the dependency of the gas transfer rate on the small scales, which coincides with Herlina and Wissink (2019).

The relationship between the gas transfer velocity k_L obtained by the DO sensor and the water depth is investigated in this section. Figure 12 (a) shows the normalized oxygen profile in the vertical direction for REF and B. The error bars show the variation of oxygen concentration at each depth. Many of the points are measured outside of the CBL, in the bulk, where the vertical oxygen concentration gradient is constant. When the probe measures sufficiently deep in the bulk, it is not as sensitive to variations in oxygen concentration due to waves compared to the CBL. Because of the waves, the reference free surface height for determining the submerging depth moves up and down. To account for this, the oxygen probe traversing depth is compensated using the wave probe readings. This tendency is displayed in Fig. 12 (a), where A and B have larger error bars than REF. Using a least-squares method, a suitable value was obtained to fit a curve to the points, $(C - C_b)/\Delta C = \exp(-y/\delta_{CBL})$. By this method, a value for δ_{CBL} is obtained for each case. In order to fit the curve, a sensitivity analysis was performed. The fit residuals were minimized, and it was desired to include a sufficient number of data points at each depth. Some of the measurement points were above the free surface, in the air, these were excluded from the fitting. The result of this analysis for each case is shown as the line in Fig. 12. Figure 12 shows that REF has a lower oxygen concentration than the other cases and that B has the highest concentration. C was excluded from this plot as the surface elevation measurements were deemed inaccurate. Therefore, the oxygen concentration at the given depths is too low. An increase in the concentration boundary layer thickness, δ_{CBL} can be seen from the values collected in Table 2 and Fig. 12 (b). There is an increase in δ_{CBL} for REF and A, and a slightly bigger one for A to B. This contradicts the results of Sanjou (2020) who reports a decreasing concentration boundary layer with increasing turbulence, but it should be noted that it has another experimental setup. Sanjou (2020) has a contraction placed in the test section to increase the turbulence between measurement locations; hence, the mean velocity is not constant everywhere in the channel. Compared to a velocity boundary layer, this study's concentration boundary layer thickness displays the same tendencies. A velocity boundary layer grows with increased free-stream turbulence (Jooss et al., 2021). The results from the concentration boundary layer indicate that the gas transfer rates increase as δ_{CBL} increases.
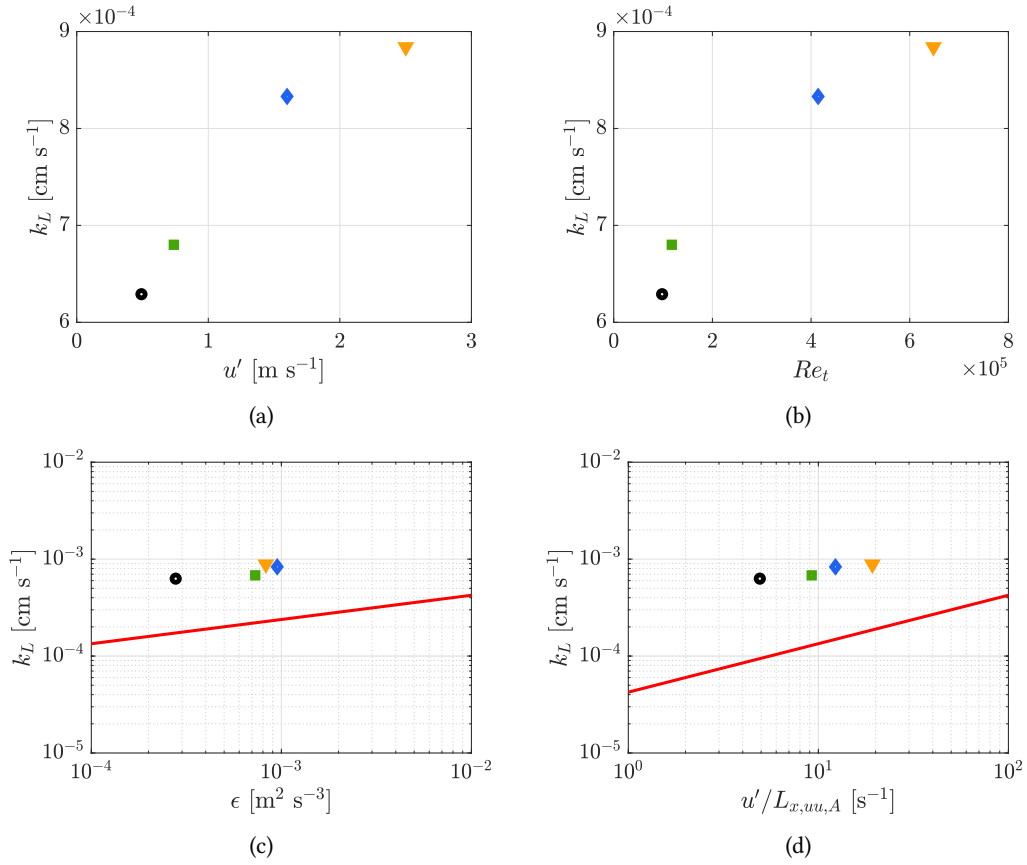
Figure 11: Obtained gas transfer rates k_L for REF ●, black; A ■, green; B ◆, blue; C ▼, orange at $95M$. The red line indicates the (c) small-eddy model and the (d) large-eddy model.
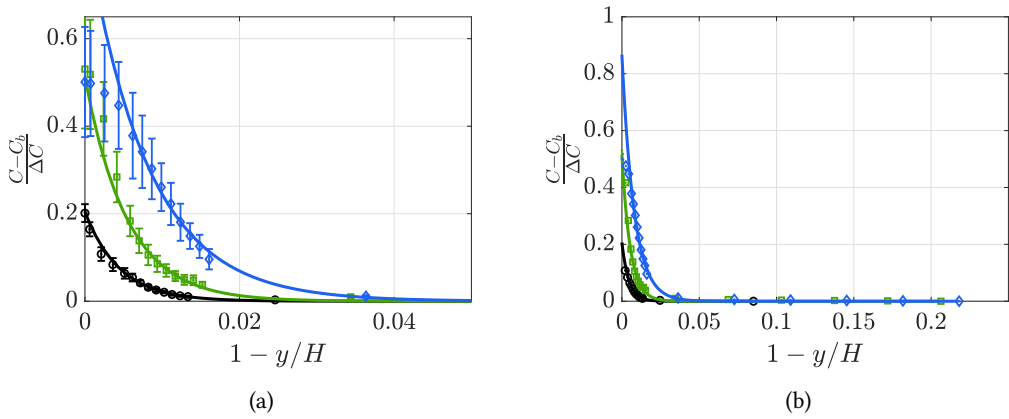

Figure 12: Vertical profile of DO in the linear reduction stage. REF ●, black; A ■, green; B ◆, blue at $95M$.
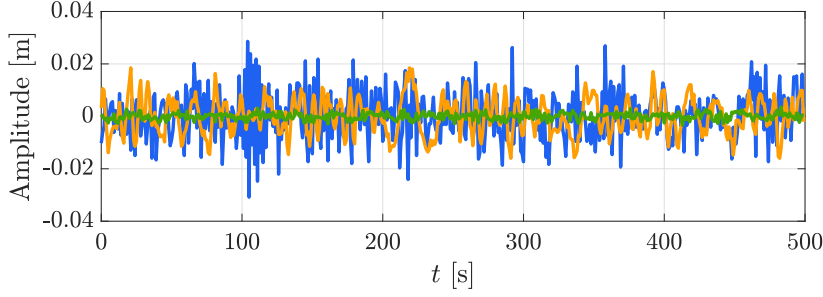
Figure 13: Wave amplitudes for A ■, green; B ◆, blue; C ▼, orange at $95M$. All values have subtracted their local mean from the 500 s timeframe.

3.3 Surface topology

The turbulence from the active grid generates surface movements of various waves of different lengths, amplitudes, and periods. The wave amplitudes for A, B and C obtained by the wave probe are presented in Fig. 13 at $95M$. The wave probe measurements were conducted close behind the oxygen probe. Wave probe measurements were not conducted for REF. The amplitudes are subtracted by the mean of the amplitude for a window of 500 s. Figure 13 indicates that A has a significantly smaller amplitude compared to B and C. This means that the surface is more still than the more turbulent cases. Case B and C appear to have a more similar signal with an amplitude at the same order of magnitude. Case B has the highest amplitude and frequency, then A and then C.

The wave spectra were calculated to investigate the waves in each case further. The wave spectra describe the distribution of energy at different frequencies. The spectra of the wave probe data are given in Fig. 14, which indicates A contains the least energy, then C, and then B with the most energy. Figure 14 shows that A, B and C have high energy for frequencies between 0.1 to 1 Hz. The energy of the waves has a strong decay from around 10 to 20 Hz. From 20 Hz, A and B display a positive gradient in the slope, meaning that energy is added to the system. The peak in B corresponds to the same frequency as the motor (0.5 ± 0.25 Hz) and could therefore result from the active grid injecting energy. For C there is also a slight increase in energy before 1 Hz, which corresponds to the frequency of the motor for this case as well (0.05 ± 0.025 Hz). C also appears to have a deeper slope between before 0.8 Hz. Figure 15 displays a histogram of each case for the amplitudes. The steepens of the slope in Fig. 14, can be due to the deviation of amplitudes as seen at 0.0025 m for C in Fig. 15. Figure 15 also displays the small amplitudes of A versus the largest ones in B. Overall, B displays the highest energy, which coincides with the frequencies displayed in Fig. 13. As wave probe measurements were not taken for REF it is not possible to compare REF and A wave results to k. However, it is possible to look into A, B, and C and their respective k. B has a high frequency, small scales, and a large increase in k compared to A. C is dominated by somewhat lower frequencies and an even more considerable increase in k compared to A. The increase between B and C is not as big as the turbulence intensity increase. Figure 14 shows that the difference in their spectra is that C carries most of its energy at low frequencies (high wavelengths).

The water surface variation for the different cases is further investigated through the data obtained from the synthetic Schlieren measurements. A larger surface area allows for a faster total diffusion rate as the free surface area to volume ratio increases, resulting in faster gas transfer. In order to investigate whether it is indeed the turbulence that influences the gas transfer rate, the surface area is studied. The surface area in this experiment was monitored by taking three independent synthetic Schlieren measurements of the surface for each case. This allows for insight into the surface deformation, and the surface area variation and roughness can be determined. The surface area was found for each of the 1500 pictures within each measurement and the mean was taken of the three independent runs. Figure 16 display an instantaneous reconstructed surface obtained by the Schlieren for all cases. The surface area parameter, γ, compares the total surface area of A, B and C to REF. The surface area parameters for all cases at $95M$ are presented in Table 2. The surface area increases by 0.02% from REF to A. Compared to this, the surface increase is larger for REF to B and C, where the surface area has increased 0.17% and 0.16%. This coincides with what Fig. 13 indicates. The maximum surface increase is 0.17 %, which is small.

In addition to the surface area increase compared to REF, the mean square slope was determined. The
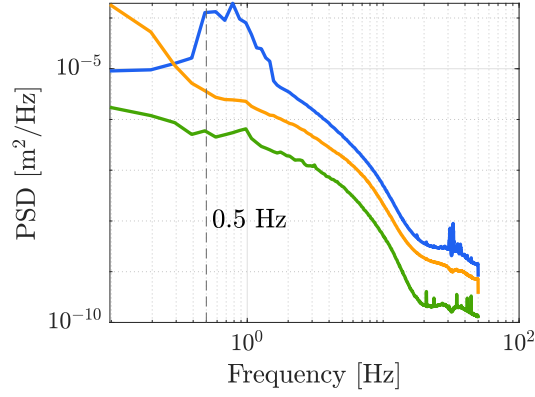
Figure 14: Power spectral density of wave amplitudes for A ■, green; B ◆, blue; C ▼, orange at $95M$.
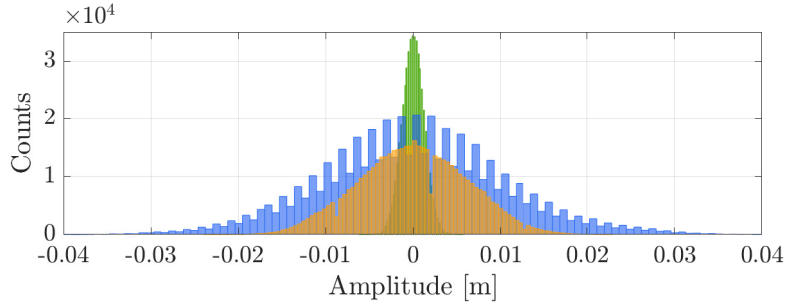

Figure 15: Histogram of the wave amplitudes of A ■, green; B ◆, blue; C ▼, orange at $95M$.

mean square slope is a key parameter when investigating the effect of a free wavy surface concerning the water-side gas transfer (Jähne et al., 1987; Zappa et al., 2004). The mean square slope $\langle S^2 \rangle$, is defined as the variance of the surface slope. In this study, the slope is calculated on the surface gradients for each case. The slope varies from 0.00002% to 0.0053% from the least to most turbulent case. This gives a surface increase under 0.5%, also very low. This supports the indications from the result of the surface area increase, as the surface variation is small. Most previous experiments on gas transfer with a similar experimental setup do not report their surface area variations, and it is therefore difficult to compare these results (e.g., Herlina and Jirka, 2008; Sanjou, 2020). Previous experiments that report their surface area variations often focus on wind effects, microbreaking, and waves, which have a significant impact the gas transfer rate. These report $\langle S^2 \rangle$ values more than an order of magnitude larger than the most turbulent case in this study (Bock et al., 1999; Zappa et al., 2004). However, since the surface area variations are so minor, the effects on the gas transfer rate are deemed negligible.
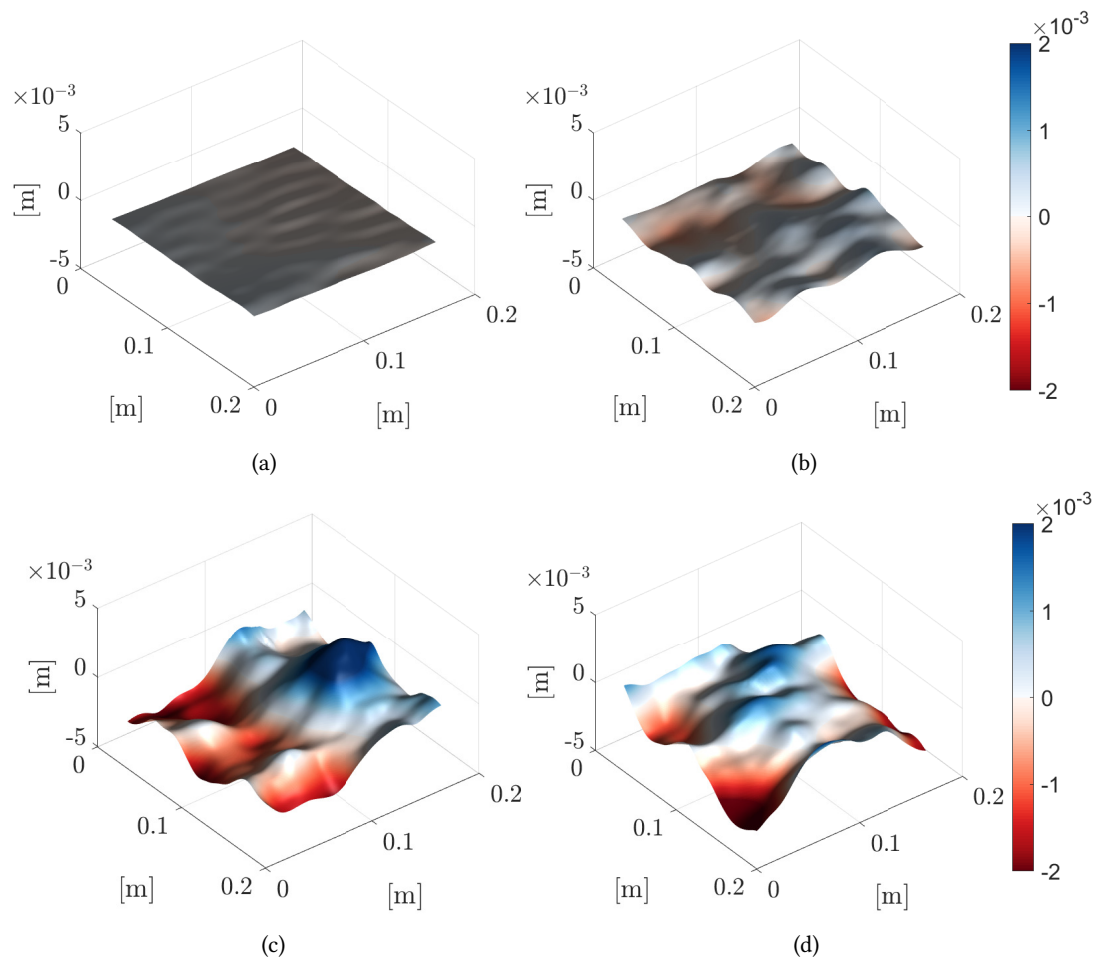
Figure 16: Instantaneous reconstructed surface from the synthetic Schlieren of (a) REF (b) A (c) B (d) C at $95M$. The colorbars are the same for each case.

4 Conclusion

An experimental setup was created to investigate the influence of turbulence on the oxygen gas transfer rate at an air-water interface. Different turbulent conditions were created by the active grid in the NTNU water channel facility. The flow conditions were measured by PIV and LDV in order to obtain the turbulence statistics and flow properties. To monitor the oxygen gas transfer rate a fine optical probe was used. A wave probe and a synthetic Schlieren method were used to record the waves and the surface area. It was possible to measure within the concentration boundary layer and satisfactorily resolve it in this investigation. These preliminary findings suggest that the concentration boundary layer was thicker in higher turbulence scenarios, but the exact relationship between higher turbulence levels in the flow, higher values of gas transfer rates, and thicker boundary layers remains unknown. The present study indicates that the oxygen gas transfer rate is influenced by turbulence. There appears to be a trend where increasing turbulence gives a higher gas transfer rate. From the observations in this study, there is an indication that the eddy sizes play a role in the gas transfer rate. The measured gas transfer coefficients k_L and k_2 showed a general trend where the gas transfer rate was influenced by smaller scales, and coincided better with the small-eddy model than the large-eddy model. The surface area variation and mean squared slope revealed that there were negligible variations in the surface area for the cases with different turbulent intensities in this study. All these interrelated facts suggests that the gas transfer rate is governed by the turbulence intensity and the eddy sizes. The results obtained indicate that the contribution of the small eddies to the gas transfer is more significant, but that the dependency of this is difficult to conclude on.

Bibliography

Adrian, R. & Yao, C. (1986). Power spectra of fluid velocities measured by laser Doppler velocimetry. *Experiments in Fluids*, *5*(1), 17–28.

Banerjee, S., Scott, D. & Rhodes, E. (1968). Mass transfer to falling wavy liquid films in turbulent flow. *Industrial & Engineering Chemistry Fundamentals*, *7*(1), 22–27.

Bock, E. J., Hara, T., Frew, N. M. & McGillis, W. R. (1999). Relationship between air-sea gas transfer and short wind waves. *Journal of Geophysical Research: Oceans*, *104*(C11), 25821–25831.

Boyer, L. & Searby, G. (1986). Random sampling: Distortion and reconstruction of velocity spectra from fast fourier-transform analysis of the analog signal of a laser Doppler processor. *Journal of Applied Physics*, *60*(8), 2699–2707.

Brumley, B. H. & Jirka, G. H. (1987). Near-surface turbulence in a grid-stirred tank. *Journal of Fluid Mechanics*, *183*, 235–263.

Castro, I. P. & Vanderwel, C. (2021). Turbulent flows: An introduction.

Cengel, Y. & Cimbala, J. (2013). *Ebook: Fluid mechanics fundamentals and applications (si units)*. McGraw Hill.

Christensen, K. T. & Wu, Y. (2005). Characteristics of vortex organization in the outer layer of wall turbulence. *Fourth international symposium on turbulence and shear flow phenomena*.

Chu, C. R. & Jirka, G. H. (1992). Turbulent gas flux measurements below the air-water interface of a grid-stirred tank. *International Journal of Heat and Mass Transfer*, *35*(8), 1957–1968.

Copeland, B. & Duffer, W. R. (1964). Use of a clear plastic dome to measure gaseous diffusion rates in natural waters. *Limnology and Oceanography*, *9*(4), 494–499.

Danckwerts, P. (1951). Significance of liquid-film coefficients in gas absorption. *Industrial & Engineering Chemistry*, *43*(6), 1460–1467.

Doda, B. (2008). *Ldv-laser Doppler velocimetry*. Retrieved 15th December 2021, from https://velocimetry.net/ldv_principles.htm

Dogan, E., Hearst, R. J., Hanson, R. E. & Ganapathisubramani, B. (2019). Spatial characteristics of a zero-pressure-gradient turbulent boundary layer in the presence of free-stream turbulence. *Physical Review Fluids*, *4*(8), 084601.

Doran, P. M. (2013). Chapter 7 - fluid flow. In P. M. Doran (Ed.), *Bioprocess engineering principles (second edition)* (Second Edition, pp. 201–254). Academic Press. https://doi.org/https://doi.org/10.1016/B978-0-12-220851-5.00007-1

Fortescue, G. & Pearson, J. (1967). On gas absorption into a turbulent liquid. *Chemical Engineering Science*, *22*(9), 1163–1176.

Gulliver, J. S. & Halverson, M. J. (1989). Air-water gas transfer in open channels. *Water Resources Research*, *25*(8), 1783–1793.

Hearst, R. J. & Lavoie, P. (2015). The effect of active grid initial conditions on high Reynolds number turbulence. *Experiments in Fluids*, *56*(10), 1–20.

Herlina, H. & Jirka, G. H. (2008). Experiments on gas transfer at the air–water interface induced by oscillating grid turbulence. *Journal of Fluid Mechanics*, *594*, 183–208.

Herlina, H. & Wissink, J. G. (2019). Simulation of air–water interfacial mass transfer driven by high-intensity isotropic turbulence. *Journal of Fluid Mechanics*, *860*, 419–440.

Higbie, R. (1935). The rate of absorption of a pure gas into a still liquid during short periods of exposure. *Trans. American Institute of Chemical Engineers*, *31*, 365–389.

Hopfinger, E. & Toly, J.-A. (1976). Spatially decaying turbulence and its relation to mixing across density interfaces. *Journal of Fluid Mechanics*, *78*(1), 155–175.

Ikeda, Y., Nishigaki, M., Ippommatsu, M. & Nakajima, T. (1994). Optimum seeding particles for successful laser Doppler velocimeter measurements. *Particle & particle systems characterization*, *11*(2), 127–132.

Jähne, B., Münnich, K. O., Bösinger, R., Dutzi, A., Huber, W. & Libner, P. (1987). On the parameters influencing air-water gas exchange. *Journal of Geophysical Research: Oceans*, *92*(C2), 1937–1949.

Jooss, Y., Li, L., Bracchi, T. & Hearst, R. J. (2021). Spatial development of a turbulent boundary layer subjected to freestream turbulence. *Journal of Fluid Mechanics*, *911*.

Lamont, J. C. & Scott, D. (1970). An eddy cell model of mass transfer into the surface of a turbulent liquid. *American Institute of Chemical Engineers Journal*, *16*(4), 513–519.

Laskari, A., de Kat, R., Hearst, R. J. & Ganapathisubramani, B. (2018). Time evolution of uniform momentum zones in a turbulent boundary layer. *Journal of Fluid Mechanics*, *842*, 554–590.

Lavoie, P., Djenidi, L. & Antonia, R. (2007). Effects of initial conditions in decaying turbulence generated by passive grids. *Journal of Fluid Mechanics*, *585*, 395–420.

Lewis, W. K. & Whitman, W. G. (1924). Principles of gas absorption. *Industrial & Engineering Chemistry*, *16*(12), 1215–1220.

Lindken, R. & Burgmann, S. (2012). Laser-optical methods for transport studies in low temperature fuel cells. *Polymer electrolyte membrane and direct methanol fuel cell technology* (pp. 425–461). Elsevier.

Makita, H. (1991). Realization of a large-scale turbulence field in a small wind tunnel. *Fluid Dynamics Research*, *8*(1-4), 53.

McBride, G. B. & Chapra, S. C. (2005). Rapid calculation of oxygen in streams: Approximate delta method. *Journal of Environmental Engineering*, *131*(3), 336–342.

McCready, M., Vassiliadou, E. & Hanratty, T. (1986). Computer simulation of turbulent mass transfer at a mobile interface. *American Institute of Chemical Engineers Journal*, *32*(7), 1108–1115.

McKenna, S. & McGillis, W. (2004). The role of free-surface turbulence and surfactants in air–water gas transfer. *International Journal of Heat and Mass Transfer*, *47*(3), 539–553.

Moisy, F., Rabaud, M. & Salsac, K. (2009). A synthetic Schlieren method for the measurement of the topography of a liquid interface. *Experiments in Fluids*, *46*(6), 1021–1036.

Nore, A. (2021). An experimental set-up to investigate the far-field decay of turbulence. *Project work, NTNU*.

O'Neill, P. L., Nicolaides, D., Honnery, D., Soria, J. et al. (2004). Autocorrelation functions and the determination of integral length with reference to experimental and numerical data. *15th Australasian fluid mechanics conference*, *1*, 1–4.

Paul, A., Laurila, T., Vuorinen, V. & Divinski, S. V. (2014). Fick's laws of diffusion. *Thermodynamics, diffusion and the Kirkendall effect in solids* (pp. 115–139). Springer.

Plate, E. & Friedrich, R. (1984). Reaeration of open channel flow. *Gas transfer at water surfaces* (pp. 333–346). Springer.

Prentice, I. C., Farquhar, G., Fasham, M., Goulden, M., Heimann, M., Jaramillo, V., Kheshgi, H., Le Quéré, C., Scholes, R., Wallace, D. W. et al. (2001). The carbon cycle and atmospheric carbon dioxide.

Sanjou, M. (2020). Local gas transfer rate through the free surface in spatially accelerated open-channel turbulence. *Physics of Fluids*, *32*(10), 105103.

Savelsberg, R. & Van De Water, W. (2009). Experiments on free-surface turbulence. *Journal of Fluid Mechanics*, *619*, 95–125.

Thackston, E. L. & Krenkel, P. A. (1969). Reaeration prediction in natural streams. *Journal of the Sanitary Engineering Division*, *95*(1), 65–94.

Theofanous, T., Houze, R. & Brumfield, L. (1976). Turbulent mass transfer at free, gas-liquid interfaces, with applications to open-channel, bubble and jet flows. *International Journal of Heat and Mass Transfer*, *19*(6), 613–624.

Tropea, C., Yarin, A. L., Foss, J. F. et al. (2007). *Springer handbook of experimental fluid mechanics* (Vol. 1). Springer.

Tsivoglou, E., O'Connell, R., Walter, C., Godsil, P. & Logsdon, G. S. (1965). Tracer measurements of atmospheric reaeration: I. laboratory studies. *Journal (Water Pollution Control Federation)*, 1343–1362.

Turney, D. E. & Banerjee, S. (2013). Air-water gas transfer and near-surface motions. *Journal of Fluid Mechanics*, *733*, 588–624.

Turney, D. E., Smith, W. C. & Banerjee, S. (2005). A measure of near-surface fluid motions that predicts air-water gas transfer in a wide range of conditions. *Geophysical Research Letters*, *32*(4).

Wallingford, H. (2021). *Data acquisition software (hr daq)*. Retrieved 15th December 2021, from https://equipit.hrwallingford.com/hydraulic-lab-equipment/data-acquisition-software-hr-daq

Zappa, C. J., Asher, W. E., Jessup, A. T., Klinke, J. & Long, S. (2004). Microbreaking and the enhancement of air-water transfer velocity. *Journal of Geophysical Research: Oceans*, *109*(C8).

Appendix

A   Spectrum of velocity fluctuations

The spectral analysis is limited to the low frequency and sampling rate of the PIV and LDV. As previously mentioned, the PIV data in this study have a sampling frequency of 2 Hz. This is too low to resolve the temporal evolution of the flow, as each image is taken too long after the previous one, and the result is independent images of the flow. Therefore, the velocity spectrum are calculated for the streamwise velocity time series obtained by the LDV. A fast Fourier transform computes the spectrum. Furthermore, a windowing function was used to reduce noise, which excludes parts of the larger scales of the flow. The velocity spectrum for each case are given in Figure 17. The sampling time period of the LDV was low and therefore the large scale structures are not present in Figure 17. In addition to this, the sampling frequency was too low to display the smallest scales, the Kolmogorov scales. The LDV was captured near the surface, and thus it could be that the results display not only turbulence but also surface effects. REF and A have similar tendencies up until approximately a frequency of $10^{2.2}$ where REF becomes steeper, while A is flattening out together with B and C. B and C separate from REF and A by containing more energy for the lower frequenciess.
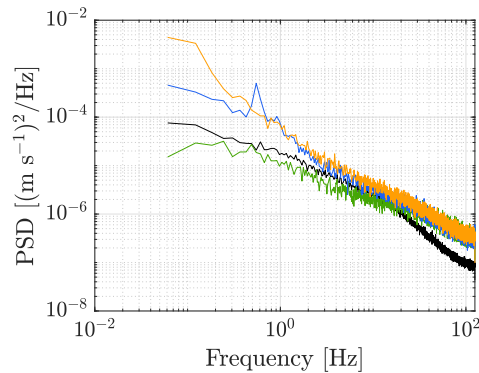

Figure 17: Power spectral density for REF ●, black; A ■, green; B ◆, blue; C ▼, orange at $95M$.

B   Surface wedge

The active grid in the NTNU water channel generates some surface motions and air entrainment. From previous experience, it has been observed that the active grid entrains air into the water. It is important to avoid measuring the impact of the active grid directly, this study wants to isolate the effects of the turbulence. Therefore, a wedge was designed to be placed at the water surface around the rods of the active grid. The wedge spanned almost the entire width of the water channel, and was 0.6 m long towards the test section, and 0.38 m long in the other direction. The design resembled Savelsberg and Van De Water (2009) installation as presented in their Figure 1. It was a big installation, and unfortunately, due to time limitations and work overload for the technical personnel, it was not finished until the experiments were conducted. The design of the wedge is given in Figure 18 for reference.
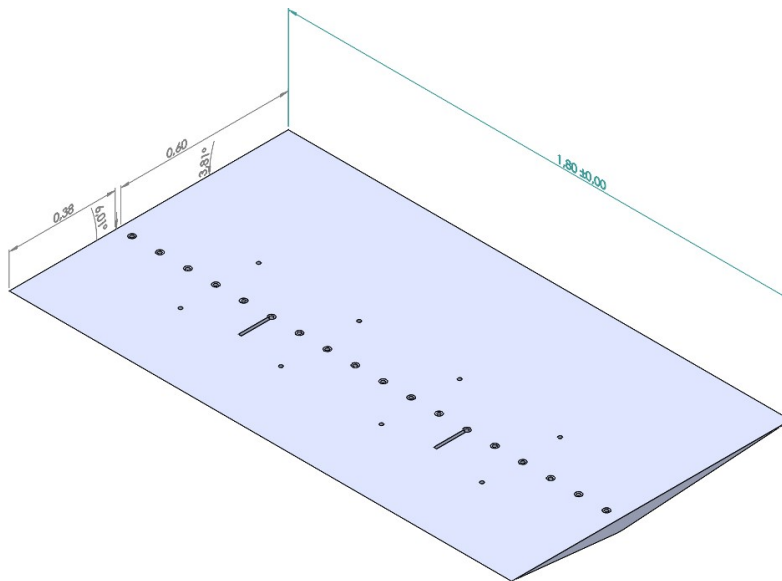
(a)
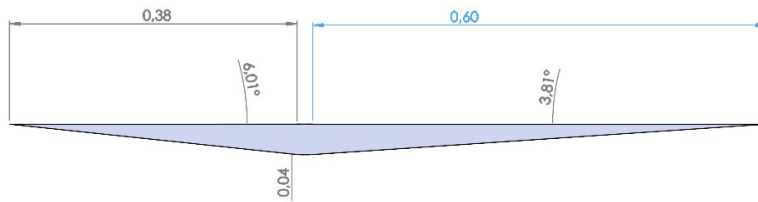
(b)

Figure 18: SolidWorks drawing of design of the wedge with dimensions. (a) Perspective view (b) side view.